Unmanned Aerial Sensor Placement for Cluttered Environments

André Farinha, Raphael Zufferey, Peter Zheng, Sophie F. Armanini, and Mirko Kovac

***Abstract*—Unmanned aerial vehicles (UAVs) have been shown to be useful for the installation of wireless sensor networks (WSNs). More notably, the accurate placement of sensor nodes using UAVs, opens opportunities for many industrial and scientific uses, in particular, in hazardous environments or inaccessible locations. This publication proposes and demonstrates a new aerial sensor placement method based on impulsive launching. Since direct physical interaction is not required, sensor deployment can be achieved in cluttered environments where the target location cannot be safely approached by the UAV, such as under the forest canopy. The proposed method is based on mechanical energy storage and an ultralight shape memory alloy (SMA) trigger. The developed aerial system weighs a total of 650 grams and can execute up to 17 deployments on a single battery charge. The system deploys sensors of 30 grams up to 4 meters from a target with an accuracy of $\pm$ 10 cm. The aerial deployment method is validated through more than 80 successful deployments in indoor and outdoor environments. The proposed approach can be integrated in field operations and complement other robotic or manual sensor placement procedures. This would bring benefits for demanding industrial applications, scientific field work, smart cities and hazardous environments [Video attachment: https://youtu.be/duPRXCyo6cY].**

***Index Terms*—Aerial systems, applications, robotics in hazardous fields, sensor networks.**

Manuscript received February 24, 2020; accepted July 21, 2020. Date of publication August 11, 2020; date of current version August 25, 2020. This letter was recommended for publication by Associate Editor J. Roberts and Editor P. Pounds upon evaluation of the Reviewers' comments. This work was supported by NERC and NPIF under Grant NE/R012229/1, and carried out within the framework of the EURO fusion Consortium; the Euratom research and training programme 2014–2018. The views and opinions expressed herein do not necessarily reflect those of the European Commission. As well as 2019–2020 under Grant 633053, and in part by NERC [NE/L002515/1] and the Grantham Institute - Climate Change and the Environment, Imperial College London; the South East Asia Rainforest Research Partnership; the Engineering and Physical Sciences Research Council (EP/R009953/1, EP/N018494/1, EP/R026173/1, EP/S031464/1); the EU H2020 AeroTwin project under Grant ID 810321. The work of Mirko Kovac is supported by the Royal Society Wolfson fellowship (RSWF/R1/18003). The Multi-Terrain Aerial Robotics Arena is supported through a philanthropic gift by Brahmal Vasudevan. *(Corresponding author: André Farinha).*

André Farinha, Raphael Zufferey, and Sophie F. Armanini are with Aerial Robotics Laboratory, Imperial College London, London SW7 2AZ, U.K. (e-mail: a.farinha17@imperial.ac.uk; r.zufferey16@imperial.ac.uk; s.f.armanini@tudelft.nl).

Peter Zheng is with Aerial Robotics Laboratory, Imperial College London, London SW7 2AZ, U.K., and also with Science and Solutions for a Changing Planet DTP, Grantham Institute Climate Change and the Environment, London WC2A 3PH, U.K. (e-mail: peter.zheng13@imperial.ac.uk).

Mirko Kovac is with Aerial Robotics Laboratory, Imperial College London, London SW7 2AZ, U.K., and also with Materials and Technology Centre of Robotics, Swiss Federal Laboratories for Materials Science and Technology, 8600 Dübendorf, Switzerland (e-mail: m.kovac@imperial.ac.uk).

This article has supplementary downloadable material available at https://ieeexplore.ieee.org, provided by the authors.

Digital Object Identifier 10.1109/LRA.2020.3015459

I. Introduction

WIRELESS sensor networks (WSNs) are a remote sensing framework that can operate over relatively large spatial and temporal scales. This is achieved through the usage of low cost and low power sensors with limited communication ranges, densely distributed throughout a physical space. Communication strategies between nodes are an established research topic that uses low energy communications to create a data forwarding mesh, through which the acquired information is transmitted to data sinks and then uploaded to a server.

The use of robotics for WSNs can bring improvements in terms of reliability and data yield, which is strongly affected by environmental conditions. In fact, the usage of sensor networks in the field is far from fail-proof: their deployment is very labor-intensive and unforeseen environmental conditions commonly lead to errors and, therefore, reductions in the data yield as high as 98% [1]. This is a research topic that is still in its infancy and even though the major challenges and opportunities are becoming clear, few systems have been tested. While most work, [2]–[4] has focused on the architecture of a flexible network whose structure adapts to newly deployed sensors and to the presence of UAVs as mobile agents, some recent research, [5]–[7] reports on the development of new sensor delivery methods.

The deployment systems in [2], [5] make use of a mechanism that consists of an auger actuated by a servomotor with the sensor nodes attached between the loops. This allows for multiple sensors to easily be stored on-board and dropped from flight. The survival of the sensor node has also been an area of interest. Sensor packaging has been shown to absorb the ground impact energy [3], while the use of an aerial breaking system inspired by Samara seeds reduces the impact speed [5].

The "drop from flight" approach used in most previous research is a viable approach for scenarios where the aim is to deploy large scale networks, as the precision in placement of the sensor is normally not critical. In these scenarios, the scaling of the cost per node is detrimental for a network to be economically viable [5], thus, a method that does not require extra attachment mechanisms per node is advantageous.

However, drop from flight deployment is often not applicable to industrial sensing cases and other field studies where precise placement of the sensors is required. For example, the usage of WSNs in oil rigs and wind farms has been demonstrated in the field to reduce their high maintenance costs [8]. This has been shown for a manually controlled UAV deploying a NDE sensor into a flat metal plate and a metal pipe using a passive contact release gripper [6]. Another study shows sensor placement in trees using an aerial manipulator with simulated compliance [7].

Another application of interest are nuclear fusion reactors. Even though this technology is still not fully ready for

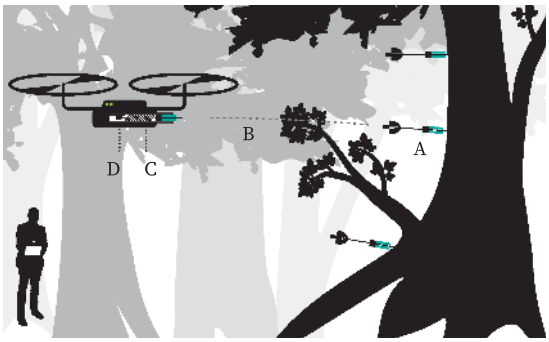

Fig. 1. Impulsive aerial sensor launching method for sensor installation at height has applications in forested environments. The relevant elements covered are: sensor attachment (A), sensor trajectory (B), energy storage (C) and trigger mechanism (D).

commercial use, current reactors such as EURO fusion's JET tokamak and ITER have the potential to achieve controlled fusion burn [9]. However, a fully functioning nuclear reactor will produce high levels of radiation and contamination, making human maintenance in the facility impossible. There is thus a need for the development of robotic and autonomous maintenance systems. Current systems consist of remotely operated robots that perform a wide variety of tasks [10]. The maintenance tasks performed by these robots are complex and can benefit from the usage of UAVs as a fast inspection, surveying and sensing tool.

Likewise, placing sensors at know heights within forests requires some degree of accuracy. In fact, forest canopy imposes a strong buffering effect on microclimate conditions beneath it, which is essential for the survival of these ecosystems [11]. A system that can deploy sensors at different heights in compact forests can allow researchers to quantify this phenomenon.

This article proposes a novel approach to remote sensor placement, keeping a safe distance to the target without compromising precision. This is achieved by impulsively launching the sensor in flight, owing to a small form factor mechanism that both stores and releases the necessary energy. We discuss the relevant theory and practical considerations to understand, design and demonstrate this method, illustrated in Fig. 1.

Section II presents a brief overview of existing sensor delivery strategies, motivating the new approach proposed. The requirements for attachment to a tree or metallic structure are defined in Section III. Based on this information, accurate trajectory planning and launch energy storage methods are discussed in Sections IV and V. The energy stored mechanically in the spring system is released via an SMA trigger mechanism designed and modelled in Section VI. The launching mechanism was tested in flight. Indoor deployment, with closed-loop position control, was conducted to quantify the dispersion pattern. Qualitative flight tests were conducted outdoors with manual piloting to further assess the robustness of the platform. The results are shown in Section VII.

Integrating the proposed mechanism with a standard quadrotor control and navigation framework will result in a fully-fledged, autonomous and robust sensor-launching system, enabling many new real-world applications.

II. Sensor Delivery Methods

This section discusses the two sensor placement methods studied thus far in the literature, i.e. direct surface interaction and drop from height. The proposed alternative approach of impulsive deployment is then introduced and motivated. The main features of all three approaches are presented in the table below Fig. 2.

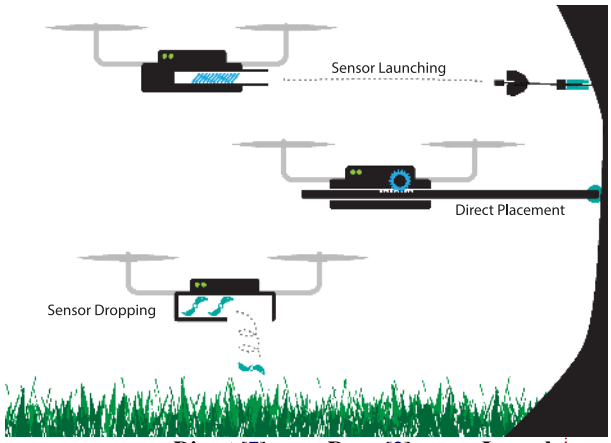

	Direct [7]	**Drop** [2]	**Launch** [i]
Accuracy	±0.025 m	±4 m	±0.1 m
Safety distance	0 m	>10 m	4 m
Payload	1.85 kg	10 kg [ii]	0.65 kg
Sensor number	single	multiple	expandable

Fig. 2. Aerial sensor placement methods for sensor installation.

TABLE I
Estimated Indentation Energy for Wood [21]

	Red Pine	Birch	Chestnut	Oak	Willow
Wood	7.25 J	8.76 J	8.31 J	12.68 J	7.10 J
Bark	0.87 J	1.05 J	1.00 J	1.53 J	0.85 J

A. Direct Placement

The usage of manipulators is a viable method for sensor delivery. This is a well-developed field whose contributions can be directly applied to sensor placement [12]. The added mass of a manipulator, however, means mission lengths are shorter and flight is more unstable due to the off-centered mass of the manipulator, [13]. Moreover, operation at close proximity carries high risk factors. Accurate state estimation is required to ensure stability of the platform [14]. Sudden events, such as gusts or falling debris, may cause irrecoverable crashes. These penalties are often compounded by the need to use larger platforms to accommodate ample computing resources.

B. Sensor Dropping

In order to be able to drop sensors in an accurate manner, a sensor pod should be equipped with control surfaces so that it can change its trajectory to reach a target. This can take the form of a sensor pod such as the one in [5], with some guidance capability such as the microglider in [15]. The usage of biodegradable materials, low-cost and low-power actuation, as well as laminate manufacturing, could potentially bring the costs of such smart sensors down. This method is the simplest to implement due to the launcher aircraft's large standoff distance from obstacles.

[i] This work.
[ii] Estimated from [2].

For field operation, it is also the most robust, owing to the limited need of heavy computation and automation.

C. Impulsive Launching

Impulsive sensor deployment (or launching) can achieve a good compromise between placement accuracy and clearance from obstacles. This is a method that to the best of our knowledge has not been studied thus far in the literature. However, it is a highly promising option for UAV sensor placement operations in environments that would otherwise be considered too risky. When compared to direct placement, one can expect lower accuracy. While direct sensor placement methods suffer mostly from uncertainty in the state estimation of the UAV, the later has the added component of the trajectory of the sensor, as well as the effect of pitch oscillation at the moment of launching.

In order to be used in the field, such an impulsive system should be capable of operating in cluttered environments and deploying sensors within a radius smaller that the smallest feature where a measurement is necessary. These features are taken as an approximately 20 cm tree branch, a 30 cm oil rig pipe or an analogous active gas pipe with a potential leak. The task should be achieved with a clearance of up to 3 m from the target to keep the aircraft further away from potential obstacles in the environment. Furthermore, the mass of the system is required to stay below 1 kg to keep the UAV as small and nimble as possible. A payload of 30 g is set for the sensor and peripherals to be deployed which has been shown to accommodate microcontrollers and batteries available today.

III. Sensor Attachment

Depending on the application scenario, the surfaces where the sensors are to be attached will have different morphologies. In the offshore environment one can expect steel as the main construction material, therefore magnets are a good method of attachment. Surfaces of interest are likely to be smooth and possibly curved. In the nuclear environment, surfaces are likely to be ceramics, such as concrete, or non ferromagnetic metals suitable for fusion environments, such as Beryllium. Here, adhesives, chemical bonding and microspine mechanisms [16], [17] are the methods most likely to be successful. In a forested environment, the interest is in attaching to wood, for which penetrating spines have been shown to be a good candidate [18]. Given that this last option requires the most contact force on impact, energetic considerations in this paper are based on it.

The energy necessary to penetrate wood can be decomposed into energy expended in indentation at the tip of the indenter, and energy expended in friction by the body of the indenter in (1).

$$U_{pen} = \int_{\delta} F_{ind} + F_{fric}\, d\delta \tag{1}$$

It has been shown that the minimum uniform pressure of a conical indenter occurs for 20° to 30° cone angle [19]. The value of uniform indenting pressure varies strongly with friction, which was taken as half the maximum Coulomb friction ($0.5\sigma_y$). This yields $3\sigma_y$ for the uniform indenting pressure, where σ_y is the material's shear strength. The spine radius is a function of δ in the cone region of the indenter. Finally, assuming half the maximum Coulomb friction, the second term is obtained.

$$F_{ind} = 3\sigma_y \pi r^2(\delta)$$

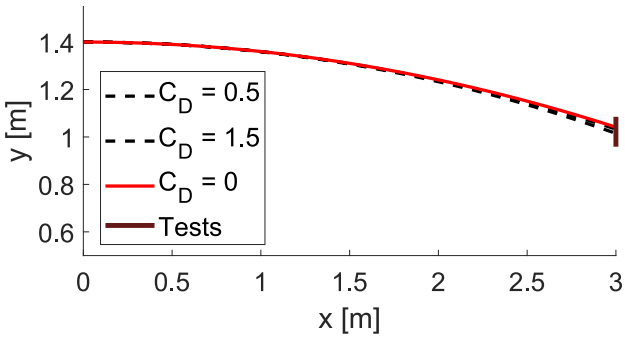

Fig. 3. Estimated trajectories for a 24 gram sensor modelled as a point mass under the influence of drag with drag coefficients of 0.5 to 1.5 and as a ballistics object. Range of impact locations of sensor placement tests are shown at the end plane of the trajectory.

$$F_{fric} = \frac{\sigma_y}{2} 2\pi R\delta \tag{2}$$

By taking data for common wood types, one can obtain the energy levels required for at least 4 mm of indentation as shown in Table I. These estimates indicate that this process requires a considerable amount of energy, which poses safety concerns for flight. However, since the sensor will often only need to perch to tree bark, the required amount of energy is actually smaller. Mechanical data on wood bark is scarce, however, results in [20] show that oak's bark shear strength is approximately 12% that of its wood and this ratio is adopted throughout.

IV. Sensor Trajectory

The flight of the projectile is influenced by the action of gravity and drag, as well as pitch, yaw and roll stability. Here, only a planar trajectory under the effect of weight and drag is considered and the equations of motion decoupled as in (3). Pitch is thus only considered for static stability and the sizing of tail stabilisers.

$$m \cdot \boldsymbol{a} = \boldsymbol{W} + \boldsymbol{D} \tag{3}$$

This equation can be integrated to obtain the trajectory of a sensor in flight. However, one of the boundary conditions is the kinetic energy at impact. Since the relation between initial and final velocity is monotonic, we use simple convex optimisation to obtain the initial value. Taking a payload of 15–30 grams, a sphere of 25 mm diameter and drag coefficients ranging from 0.5 to 1.5 ($Re \sim 10^4$) one obtains that the kinetic energy at launch must be in the order of 0.94 J to 1.74 J for the considered wood barks and a 3 meter flight.

In order to achieve accurate sensor deployment, we must estimate the sensor trajectory with external ballistic calculations. This however, incurs a certain amount of error due to the unaccounted variance in the launcher. In Fig. 3 are shown predicted ballistic trajectory with the bounds of estimated drag, as well as experimental results from flight. These results show that even though drag has some effect, it is likely not the crucial source of uncertainty in placement location.

V. Energy Storage

The critical feature when choosing a sensor launching system for aerial sensor placement is the energy storage mode. Different

approaches have been used in aerial robots for applications such as anchor launching [22]. Propellant based systems, although energy dense, require chemicals and tight tolerance components. This adds substantial complexity to the manufacturing process and limits the ability for in-field repairs. Similarly, other pneumatic systems, such as compressed gas launchers, need heavy high pressure gas-sealing components. For deployment on a compact and lightweight UAV, where payload weight severely limits flight endurance, mechanical launch is deemed to be the optimal solution. Mechanical systems are also simple to reload, repair, and are more tolerant to defects.

A first screening of energy storage modes can be done by evaluating the specific energy of each mode, while design constraints are evaluated on a later stage. The methods evaluated here make use of mechanical energy stored as strain energy. This can be done by using linear springs, bending elements, buckling elements or hyperelastic elements.

Energy storage due to bending is given by (4) where we consider a linear cantilever beam vertically loaded at the free end, and the maximum stress in the system as $\sigma_m = Plt/I$.

$$U_{el} = \frac{3EI}{2\,L^3}\delta^2 \tag{4}$$

Energy storage due to buckling can be approximated by (5), which corresponds to a thin column storing energy under the constant Euler load. The maximum deflection in buckling is not straightforward to obtain as the full elastica solution must be calculated. This requires the evaluation of elliptic integrals that can be approximated by their Taylor expansion. As shown in [23], an approximate closed form solution can be obtained and the maximum deflection calculated by solving (6) for δ.

$$U_{el} = \frac{\pi^2 EI}{L^2}\delta \tag{5}$$

$$\frac{2I\sigma_y}{tP_{crit}l} = \sqrt{\frac{80\delta/l}{\pi\left(4-\delta/l\right)^3}} \tag{6}$$

Hyperelastic elements can suffer large deformations and thus store large amounts of energy in tension. There are a number of constitutive models for such materials. Among these, Mooney-Rivlin's model is widely used in the literature and an expression can be derived for uniaxial stress as:

$$\sigma = \frac{1}{\lambda}\left(2C_1 + \frac{2C_2}{\lambda}\right)\left(\lambda^2 - \frac{1}{\lambda}\right) \tag{7}$$

As for linear springs, the energy stored can simply be calculated as $U = 1/2k\delta^2$. Numerical solutions were obtained for these different methods, observing geometrical constraints and the physical limits of the materials. The materials chosen were CFRP for bending and buckling, natural rubber for tension and spring-steel for linear springs, due to the high energy storage modulus of these materials. The solutions obtained show that for the desired system scale ($< 120\,\mathrm{mm}$) only elastomers outperform commercially available linear springs. However, the actuation length of these solutions are still out of bounds of the desired dimensions.

Considering a perfect transfer of energy between the storage element and the sensor, the amount of energy available to the sensor can be calculated as $K = V/(1 + m_s/m_{rot})$, where the mass of the sensor and the rotorcraft are known.

VI. Trigger Mechanism

A trigger mechanism with high actuation force is necessary to rapidly release the mechanical energy stored for launching. The mechanism must also hold the sensor safely during flight and produce the necessary force to actuate the trigger release.

Shape memory alloy (SMA) actuation, characterised by high actuation force to weight ratio, is an attractive solution. Such actuators are normally sized using empirical rules provided by manufacturers. However, in order to have an accurate stroke range and a good prediction of the actuation time (which is important in flight), a detailed description of the actuator is necessary.

Nickel-Titanium SMA actuators make use of a one-way shape memory effect that occurs when the material undergoes a phase transformation from martensite to austenite. This transformation can occur by increasing temperature or decreasing stress. Some materials, such as the commercially available *Flexinol-HT* wire, undergoes two phase transformations with increasing temperature: martensite - Rhombohedric (R phase) - Austenite. However, as the R-phase is present at ambient temperatures, in practice, it's only the second transformation that is used for actuation. This process is thoroughly described in [24] where an analogy with statistical thermodynamics is explored to obtain a description of phase fraction for any given temperature-stress state. As we are only interested in the heating stage (fast repeated strokes are not required), the phase fraction can be simplified:

$$\begin{aligned} R(T,\sigma) &= \frac{1}{1 + exp(C_K \cdot (T - c\cdot\sigma - T_m))} \\ T_m &= \frac{A_s + A_f}{2} \\ C_K &= \frac{4.4}{A_f - A_s} \end{aligned} \tag{8}$$

Taking the sections of material in different phases as being arranged in series, one can obtain the stress strain relationship for any phase fraction. The constitutive relation for the R-phase takes plasticity into account [25], as a 2 segment relation with intermediate stiffness (plastic section) of $(\sigma_2 - \sigma_1)/\epsilon_r$ and final stiffness equal to the Young modulus.

$$\epsilon = (1-R)\frac{\sigma}{E_A} + R(\frac{\sigma}{E_R} + \alpha(\sigma_2 - \sigma 1) + \epsilon_r) \tag{9}$$

The length of the wire can then be obtained from the engineering strain definition and used to calculate the actuation length.

The geometry of the mechanism itself is taken as a halfway point between a classic linear bias spring in series with the wire and a thin curvature based actuator. This is achieved by using a thin cantilever spring steel beam loaded by the SMA at a certain angle β. This allows for a balance between larger displacements and low actuation forces to be obtained. We are interested in taking advantage of the non-linearity of such a system and thus a simple linear bending model is not representative. The force-displacement response of such mechanism is shown in Fig. 4C, where the system is modeled as a linear cantilever beam and as a buckled Euler element when the axial force increases above P_{crit}.

The response of the mechanism in time can be obtained by deriving a relation for temperature in time. The heat transfer rates have to be estimated, which entails convective and conductive heat losses, as well as a Joule resistive heating. Assuming

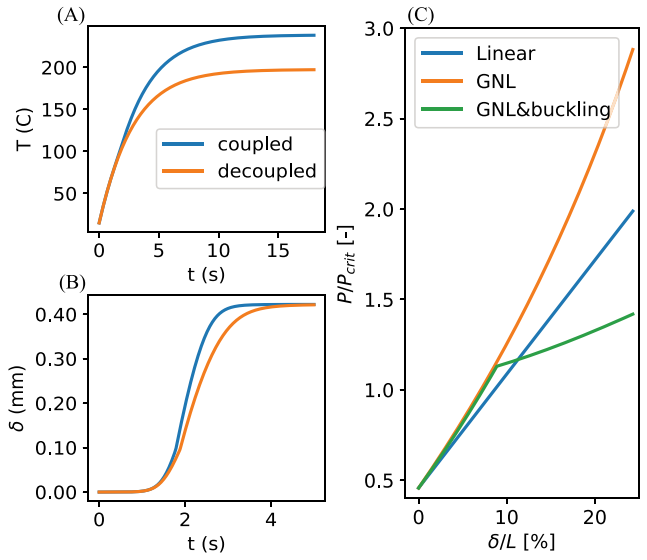

Fig. 4. Modelling of an SMA driven mechanism. (A) SMA wire temperature during actuation for a 0.25 mm diameter SMA wire, using coupled and decoupled formulation. (B) Actuation length for a planar mechanism with wire length of 20 mm and bias stress of 100 MPa using coupled and decoupled solvers. (C) Normalised actuation force and actuation length for the double bias spring setup. Results shown for linear spring model, linear spring with geometric non-linearity, and for axial force cap equal to the Euler critical load.

the temperature gradients within the wire to be negligible, we evaluate the balance of heat transfer rates from the wire as in (10). The Joule heating is obtained as $I^2 R_\rho l$, the convective heat transfer coefficient is estimated using Churchill's relation and the contact thermal resistivity is taken as an average of NiTi and steel.

$$\rho V \cdot \frac{dT}{dt} = S_J - \ddot{q}_{conv} - \ddot{q}_{cnt} \tag{10}$$

Due to the presence of the source term, there is no closed form solution for this equation and it thus needs to be integrated numerically. Despite the potentially weak coupling (thermal inertia is very low), solving the coupled system is necessary due to the varying properties of the material and heat transfer rates. As shown in Fig. 4A,B that neglecting this coupling leads to an underestimation of the steady state temperature and overestimation of the actuation period.

A sketch of the mechanism is shown in Fig. 5. As shown, there are 2 bias springs; one provides the bias force while the second buckles, creating a discontinuity in the response of the mechanism. The design of such a mechanism can be fine-tuned by varying the thickness of the the two springs, diameter of the SMA actuator wire and the value of A and β to obtain a desired behaviour. This procedure follows the following steps:

- Increase A until the desired actuation length is reached
- Starting from the lowest available actuator wire diameters:
  - Increase the thickness of the zero bias spring until the required initial stretch is reached.
  - Choose secondary bias spring so that its Euler load is higher than the zero bias load.
  - Confirm that the SMA's maximum stress is not reached an iterate if required.
- Decrease β until the Euler load is as close to the zero bias load as possible.

It is shown in Fig. 6 how the mechanism model correlates with data acquired experimentally, using visual tracking. There is approximately a 20% mismatch on the final actuation length due to slight flex of the SMA attachments. The response of the trigger with an engaged sensor is considerably different, which is expected due to the presence of friction between the sear and sear catch. This is further supported by the the presence of an inflection point, as the friction force decreases with the reduction of contact area during actuation. The non-zero derivative at start of actuation is a consequence of the difference between static and dynamic friction. Moreover, the actuation length is cut short with the sensor being disengaged from the mechanism and the launch. Even so, this shows that the presence of friction creates a 10% mismatch on the actuation time of the mechanism, which is negligible for higher driving currents.

A. *Transient Response*

The mechanism's actuation time is an important parameter for this application because of the relative motion of the UAV to the target. As the pose of the rotorcraft oscillates in time, a longer actuation time leads to more uncertainty on the pose at launch. Besides, as friction has some influence on the trigger, the actuation times are not very consistent ($\pm 0.1\Delta t$) and cannot be accounted for with a simple delay.

Experimental and calculated response times for different input current values are shown in Fig. 7A. For larger currents the trigger can be actuated faster as it takes a shorter period to supply necessary latent heat of transformation. However, due to the low thermal inertia of the actuator, the current switching has to be done precisely as to avoid burning the wire.

The trigger's response will vary with the environmental conditions due to the SMA's sensitivity to ambient temperature. The variation is estimated by performing calculations for different temperatures and varying the thermophysical properties of air accordingly. The results in Fig. 6B show a linear relationship for the actuation time and thus it is easy accounted for in the field.

VII. Deployment Tests

A. *System Setup*

A system that fulfils the requirements defined in Section I was developed in order to execute the envisioned sensor placement method in controlled indoor conditions. The same system was also used in an outdoor environment but operated in open-loop mode to examine its robustness. A schematic of the full system is shown in Fig. 5 and consists of a trigger mechanism with the necessary drivers for the SMA, a linear spring for energy storage, a sensor pod that includes the sear catch and a single spine for attachment.

As shown in Fig. 8A, a quadrotor configuration with a demonstrated maximum flight time of 16 minutes with a flight weight of 650 g is used. The system has capacity for one sensor, which is manually loaded prior to flight. A 24g sensor pod was used in the experiments, Fig. 8B,D. The pod includes the elements for the spring compression, a flight stabiliser and a capsule for the sensor. The 1.55 J of energy used for launching the sensor is stored as elastic energy with a linear spring with a maximum actuation force of 10 N. The hook (sear) is part of a single piece of steel that also comprises the bias spring and the attachment for the SMA, which is crimped to two screws that permit it's adjustment, Fig. 8C.

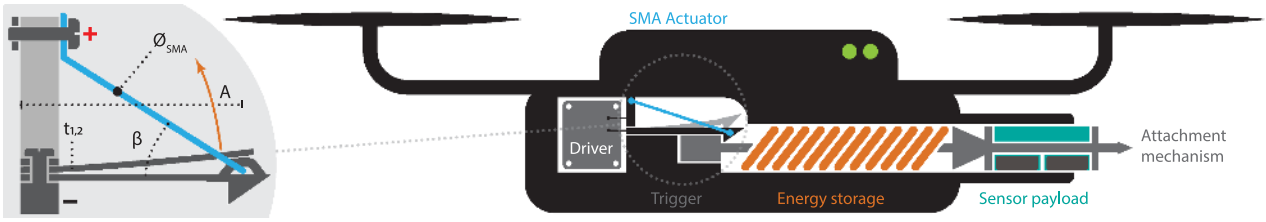

Fig. 5. Schematic of the sensor placing system with a detailed view on the trigger mechanism and its main parameters for behaviour adjustment: SMA wire diameter(Φ_{SMA}), spring length(A), springs thickness ($t_{1,2}$) and angle between the springs and the SMA wire(β).

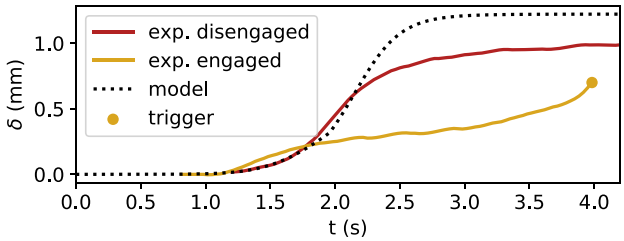

Fig. 6. Comparison of vertical displacement of the bias springs as calculated by the model and as measured experimentally using visual tracking. In red, experimental results for the disengaged mechanism and in yellow, for the mechanism engaged with a sensor pod.

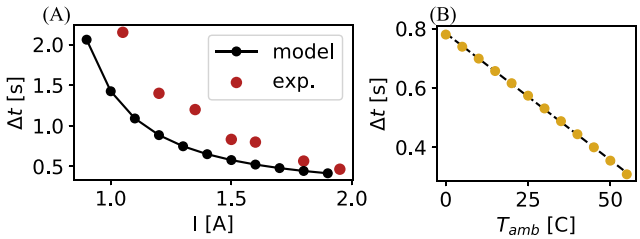

Fig. 7. (A) Comparison of experimental and theoretical results of the actuation time of the disengaged mechanism with varying driving current. (B) Evolution of actuation time with ambient temperature as calculated by the model, for a 0.25 mm diameter wire at 1.4 A current. Dashed line shows a linear fit of the simulated conditions.

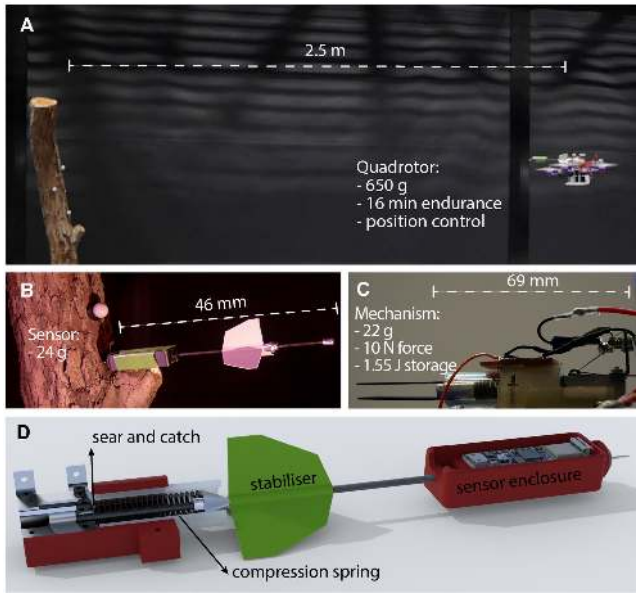

Fig. 8. Setup used for experiments. (A) Experiments carried out indoors using motion a capture system and a tree branch as the target. (B) Sensor pod for attachment in wood. (C) Launch mechanism loaded with an empty sensor pod. (D) 3D model of the launch mechanism.

In order to avoid loss of kinetic energy in components attached to the spring or in shock absorbers, the compression of the linear spring is done using the sensor housing and the trigger mechanism hooks into a nock at the back of the sensor. These components are made from 7075 Aluminium to reduce wear over multiple uses. In practice, one sensor is built for a single extended mission and can thus be built from more perishable materials. Improvements in horizontal trajectory were obtained by adding flight stabilisers to the back of the sensor pod. Experiments executed using 55 mm^2 stabilisers (a total of 3 grams added) caused the 95% confidence interval to decrease threefold for 3 m distance.

The quadrotor is flown autonomously, with position-orientation given by a motion capture system. An offboard PID position controller computes the desired roll/pitch angle, thrust, and yaw rate. The commands are then converted to PPM and sent to the flight controller via an RC transmitter. The offboard control loop runs at 50 Hz and centimeter scale setpoint tracking accuracy was achieved. Position way-points were autonomously generated to guide the quadrotor to the best launch position relative to a target detected by the motion capture system. The launch position was calculated neglecting drag or other dynamic behaviours of the sensor. Once the position is reached, the launch command is sent to the flight controller (Omnibus F4 pro running the *Betaflight* firmware). This command sets an auxiliary PWM to high, whose signal is passed through an RC filter then used to switch the SMA drive current on.

B. System Performance

There are two main performance metrics on impulsive sensor launching from an UAV. First and foremost, the success rate of placement. A failed placement may not be retrievable in some environments or might even become a hazard for industrial activities. Consequently, the precision and accuracy of system are also important because missing the target, whilst not fatal, is an unsuccessful placement.

A total of 81 successful sensor placements were executed in laboratory conditions. Two different attachment mechanisms were used throughout these experiments: a magnet for attachment on a ferromagnetic surface and a pipe of 30 cm diameter,

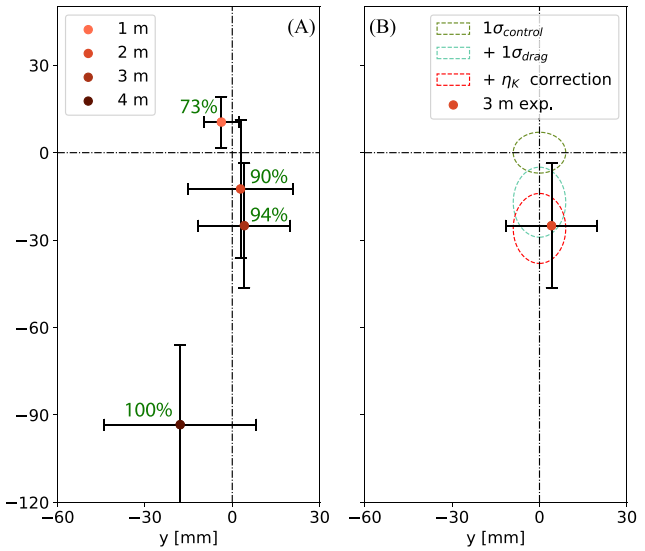

Fig. 9. Sensor placement results for the 64 tests executed on a flat metallic surface. (A) Accuracy as function of distance for a 24 gram sensor with magnetic attachment. The error bars correspond to one standard deviation on the location of the sensor on a flat metallic surface. In green, the percentage of successful placements for each distance tested. In green is shown the success rate of placement at each tested distance. (B) Illustration of the influence of imprecision on the positioning of the UAV, drag of the sensor pod and losses in potential - kinetic energy conversion.

Fig. 10. Outdoor flights in forest environment.

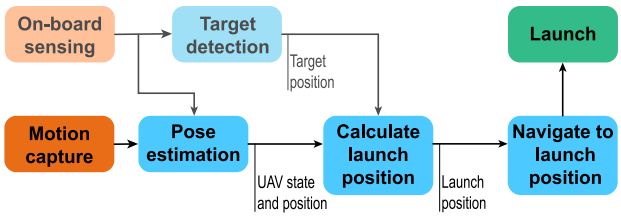

Fig. 11. Framework for field sensor placement using the proposed method. The process used for indoor experiments uses a motion capture system for pose estimation. On-board sensing for pose estimation and target detection/selection are steps necessary for field usage.

as well as a penetrating spine for attachment on a tree branch of 13 cm width.

The placements using a magnet for attachment show a clear decrease in success at close proximity due to the sensor bouncing off upon impact. Placements on the metal pipe curved surface showed lower attachment success. Two out of 5 placement attempts at 2 meter distance were unsuccessful. A total of 12 successful experiments using spine attachment were completed at distances between 2 and 4 meters from a 13 cm width branch.

The precision of this sensor placement method depends on the precision in position estimation, the pose of the vehicle and imprecision in the flight of the sensor. The first can be estimated from the accuracy of the position system used e.g. motion capture system or event camera. The second is analogous to the accuracy of the position controller used in flight, and the third is closely related to deviations from the model used to estimate the trajectory of the sensor.

Tests were performed indoors at varying distance to the target, using magnetic and spine attachment. Fig. 9A summarises 64 indoor experiments with a flat metal plate target. It is shown that accuracy in y tends to decrease with distance. This is a clear consequence of not considering drag in the trajectory estimation, as well as losses in the energy transfer between the spring and the sensor. These results can be improved by using lookup tables that take into account drag or by solving the ODE (3) in real time, and by measuring the exact launch velocity of the sensor. As for the accuracy in the x axis, the trend is not regular as this is related with pitch yaw and roll oscillations during launch. As for precision, there is a clear trend for it to drop with increased distance to the target.

The sources of inaccuracy of sensor launching at 3 meters are considered in the form of drag, controller accuracy, drag and dynamic effects at the moment of launch. Fig. 9B shows that the expected effect of oscillations in flight does not equate to the total of the experimental standard deviation and neither does the bias and uncertainty due to drag.

Analysis of high speed footage brings some insight into this discrepancy. While we here consider the conversion of kinetic energy at 90 to 95%, the footage shows that this value is actually closer to the 80% mark. This is associated with strain energy stored in deformation of the quadrotor's structure and vibration of the spring after launch. By adding this source of bias on the plot we can now account for the deviation in y of our experiments. With the placement of the launch mechanism above the center of mass, pitching of the platform was expected during launch. However, upon high-speed video analysis, we see that while the drone pitched up, the majority of the visible motion occurs after the sensor exits the mechanism.

C. *Outdoor Tests*

The system was tested in an outdoor forested location, where three trials were made. Successful attachment was performed on white birch trees at approximately 2 and 4 meters height while harder wood types did not permit reliable fixing. The deployed sensors rely on an *Arduino nano 33 BLE Sense* which streams temperature, atmospheric pressure and luminosity data over Bluetooth Low Energy.

Initial tests have shown that the proposed method can be used under manual control, due to the clearance maintained between aircraft and the target. However, regular and safe operations should be carried out autonomously, which additionally requires the usage of a state estimator and localisation, as well as a target detection system (Fig. 11). In this work, a motion capture system was used for state estimation and localisation. While this permits precise testing and quick optimisation of the system, such complex camera setups are often not available outdoors and in industrial environments.

Particularly in forests, some key challenges need to be taken into account. For instance, dense tree canopy blocks GPS signal thus making the need for alternative on-board sensors for position estimation. Vision based systems are particularly attractive, among which, visual inertial odometry (VIO) is a well developed technique [26]. As shown in Fig. 11, VIO largely functions as a direct replacement of the motion capture system. However, onboard localization systems, such as a time-of-flight sensor, stereo vision, or depth sensor, has the added benefit of providing depth information. Having knowledge of the target depth allows loop closure for the calculation of the launch position.

The need for target detection is highly dependent on the purpose of the WSN. For ecological monitoring, automated target detection and selection may lead to data bias. Therefore, manual target selection may be preferable. In this case, the depth sensor would still be beneficial in ranging, or the post-launch assessment of accuracy and the calculation of ballistic corrections. By incorporating this additional on-board sensing capability, the proposed method can effectively be deployed in challenging environments.

VIII. Conclusion

This letter presents a novel method for aerial sensor placement through impulsive launching with application to Wireless Sensor Network deployment in hazardous environments. The proposed system does not require direct physical interaction to accurately place sensors which brings significant advantages in safety as well as operation in cluttered environments.

The key aspects of designing this method are discussed, in particular energy storage methods, and the trigger that releases this energy. The micro SMA-based trigger is modeled theoretically in order to estimate actuation times and reduce uncertainty on the sensor launching. Environmental factors are taken into account so that the system can be used across a variety of climates.

The performance of the system is analysed experimentally where the main sources of uncertainty in sensor placement are identified and initial tests are carried out outdoors.

Future work will focus on improving the reliability of the method for field operations. This will required the usage of vision state estimation and positioning, as well as a depth sensor for estimation of the target location. The possibility of carrying multiple sensor on-board will also be considered.

Acknowledgment

The authors would like to thank Guy Burroughes for his helpful comments and interesting discussions concerning applications in torus reactors.

References

[1] J. Beutel, K. Römer, M. Ringwald, and M. Woehrle, *Deployment Techn. Sen. Netw.* Berlin, Heidelberg: Springer, 2009, pp. 219–248. [Online]. Available: https://doi.org/10.1007/978-3-642-01341-6_9

[2] P. Corke, S. Hrabar, R. Peterson, D. Rus, S. Saripalli, and G. Sukhatme, "Autonomous deployment and repair of a sensor network using an unmanned aerial vehicle," *IEEE Int. Conf. Robot. Autom., 2004. Proc. ICRA '04. 2004*, vol. 4, pp. 3602–3608, 2004.

[3] A. T. Erman, L. V. Hoesel, P. Havinga, and J. Wu, "Enabling mobility in heterogeneous wireless sensor networks cooperating with UAVs for mission-critical management," *IEEE Wireless Commun.*, vol. 15, no. 6, pp. 38–46, 2008.

[4] L. Bhatia, D. Boyle, and J. A. McCann, "Aerial interactions with wireless sensors," in *Proc. 16th ACM Conf. Embedded Networked Sen. Syst.*, ser. SenSys '18. New York, NY, USA: Association for Computing Machinery, 2018, pp. 373-374. [Online]. Available: https://doi.org/10.1145/3274783.3275189

[5] P. Pounds and S. Singh, "Samara: Biologically inspired self-deploying sensor networks," *IEEE Potentials*, vol. 34, no. 2, pp. 10–14, Mar. 2015.

[6] "Nde sensor delivery using unmanned aerial vehicles," *Insight - Non-Destructive Testing and Condition Monitoring*, vol. 60, no. 8, 2018.

[7] S. Hamaza *et al.*, "Sensor installation and retrieval operations using an unmanned aerial manipulator," *IEEE Robot. Autom. Lett.*, vol. 4, no. 3, pp. 2793–2800, Jul. 2019.

[8] R. A. Swartz, J. P. Lynch, B. Sweetman, R. Rolfes, and S. Zerbst, "Structural monitoring of wind turbines using wireless sensor networks," 2010.

[9] S. C. Cowley, "The quest for fusion power," *Nature Phys.*, vol. 12, no. 5, p. 384, 2016.

[10] R. Buckingham and A. Loving, "Remote-handling challenges in fusion research and beyond," *Nature Phys.*, vol. 12, no. 5, p. 391, 2016.

[11] T. Jucker and e. a. Hardwick, "Canopy structure and topography jointly constrain the microclimate of human-modified tropical landscapes," *Global Change Biology*, vol. 24, no. 11, pp. 5243–5258, 2018.

[12] F. Ruggiero, V. Lippiello, and A. Ollero, "Aerial manipulation: A literature review," *IEEE Robot. Autom. Lett.*, vol. 3, no. 3, pp. 1957–1964, Jul. 2018.

[13] P. E. I. Pounds, D. R. Bersak, and A. M. Dollar, "Stability of small-scale UAV helicopters and quadrotors with added payload mass under PID control," *Auton. Robots*, vol. 33, pp. 129–142, 2012.

[14] H. B. Khamseh, F. Janabi-Sharifi, and A. Abdessameud, "Aerial manipulation–A literature survey," *Robot. Auton. Syst.*, vol. 107, pp. 221–235, 2018.

[15] M. Kovac, A. Guignard, J. Nicoud, J. Zufferey, and D. Floreano, "A 1.5g SMA-actuated microglider looking for the light," in *Proc. IEEE Int. Conf. Robot. Autom.*, Apr. 2007, pp. 367–372.

[16] M. Kovač, J. Germann, C. Hürzeler, R. Y. Siegwart, and D. Floreano, "A perching mechanism for micro aerial vehicles," *J. Micro-Nano Mechatronics*, vol. 5, no. 3-4, pp. 77–91, 2009.

[17] M. Kovac, "Learning from nature how to land aerial robots," *Sci.*, vol. 352, no. 6288, pp. 895–896, 2016.

[18] H.-N. Nguyen, R. Siddall, B. Stephens, A. Navarro-Rubio, and M. Kovač, "A passively adaptive microspine grapple for robust, controllable perching," in *Proc. 2nd IEEE Int. Conf. Soft Robot. (RoboSoft)*. 2019, pp. 80–87.

[19] G.-J. Xiong, J.-J. Chen, J.-H. Wang, and M.-G. Li, "New axisymmetric slip-line theory for metal and its application in indentation problem," *J. Eng. Mech.*, vol. 145, no. 12, 2019, Art. no. 04019099.

[20] P. V.-I. Č.-V. Račko, "The shear strength on the wood/bark border of sessile oak."

[21] D. W. Green, J. E. Winandy, and D. E. Kretschmann, "Mechanical properties of wood," *Wood Handbook: Wood as an Engineering Material. Madison, WI: USDA Forest Service, Forest Products Laboratory, 1999. Gen. Technical Report FPL; GTR-113: Pages 4.1-4.45*, vol. 113, 1999.

[22] K. Zhang, P. Chermprayong, T. M. Alhinai, R. Siddall, and M. Kovac, "Spidermav: Perching and stabilizing micro aerial vehicles with bio-inspired tensile anchoring systems," in *Proc. IEEE/RSJ Int. Conf. Intell. Robot. Syst. (IROS)*, Sep. 2017, pp. 6849–6854.

[23] A. H. Nayfeh and S. A. Emam, "Exact solution and stability of postbuckling configurations of beams," *Nonlinear Dyn.*, vol. 54, no. 4, pp. 395–408, 2008.

[24] K. Ikuta, M. Tsukamoto, and S. Hirose, "Mathematical model and experimental verification of shape memory alloy for designing micro actuator," in *Proc. IEEE Micro Electro Mech. Syst.*, Jan. 1991, pp. 103–108.

[25] N. Troisfontaine, P. Bidaud, and M. Larnicol, "Optimal design of micro-actuators based on sma wires," *Smart Mater. Struct.*, vol. 8, no. 2, p. 197, 1999.

[26] C. Forster, L. Carlone, F. Dellaert, and D. Scaramuzza, "On-manifold preintegration for real-time visual–inertial odometry," *IEEE Trans. Robot.*, vol. 33, no. 1, pp. 1–21, Feb. 2017.